Full length article

The thickness effect of rubbery nanofibrous mat on modes I–II fracture mechanism of composite laminates

Hesamaldin Saghafi [a], Isa Ahmadi [a], Ramin Khamedi [a], Hamed Saghafi [b], Milad Saeedifar [c], Tommaso Maria Brugo [d,*], Emanuele Maccaferri [e], Jacopo Ortolani [e], Francesco Mongioì [d], Laura Mazzocchetti [e], Andrea Zucchelli [d]

[a] Department of Mechanical Engineering, Faculty of Engineering, University of Zanjan, 45371-38791, Zanjan, Iran
[b] Department of Mechanical Engineering, Tafresh University, 39518-79611, Tafresh, Iran
[c] Faculty of New Technologies and Aerospace Engineering, Shahid Beheshti University, 19839-69411, Tehran, Iran
[d] Department of Industrial Engineering, University of Bologna, Viale Risorgimento 2, 40136, Bologna, Italy
[e] Department of Industrial Chemistry, University of Bologna, Viale Risorgimento 4, 40136, Bologna, Italy

ARTICLE INFO

ABSTRACT

This study investigates the effect of the interleaving nanofibers, made of NBR/PCL blend, on the interlaminar fracture toughness of carbon/epoxy laminates. Different nanomat thicknesses, ranging from 20 μm to 120 μm, were tested at Mode-I and mode-II and results were compared to the non-modified laminates. Acoustic Emission (AE) technique was used to assess the influence of interleaving nanofibers on dominant damage modes of the specimens, i.e., matrix cracking, fiber/matrix debonding, and fiber breakage. Moreover, the damage mechanism and the nanofiber toughening contribution were investigated by means of crack path and surface analysis. Results indicated that the optimum nanomat thickness for mode-I is 40 μm ($G_{I,R} = +333$ %), while for mode-II is 20 μm ($G_{II,R} = +43$ %). The study also confirmed by AE the significant impact of nanofibers on various damage modes, especially during mode-I loading.

1. Introduction

Thermoset based composite materials are widely used in the industry due to their favorable mechanical properties, such as their high strength-to-weight ratio. Despite this advantage, there is a possibility of various failures in these materials: (1) fiber breakage, (2) matrix cracking, (3) fiber/matrix debonding, and (4) delamination [1]. Delamination is the most common type of failure in these materials, which leads to a decrease in strength and flexural modulus [2]. This is due to the low interlaminar fracture toughness of these materials.

Different methods have been proposed to hinder delamination in fiber reinforced composite materials, such as matrix toughening [3,4], optimization of stacking sequence [5–8], laminate stitching [9–11], braiding [12,13], edge cap reinforcement [14], and critical ply termination [15]. Although these methods have been effective in increasing the interlaminar fracture toughness, they reduce the in-plane properties such as compressive strength and the elastic modulus [16]. In 2001, Dzenis and Reneker presented a new method to hinder delamination by

interleaving polymeric nanofibers between composite layers. It led to increase in fracture toughness, and at the same time, did not have a negative effect on the in-plane properties of the laminate [17]. Since then, many researchers have studied this new method and made different polymeric nanofibers such as Nylon [18–21], Polysulfone [22–25], Polyvinylidene fluoride [26], Polyvinyl butyral [27,28] and Polycaprolactone [29,30] to investigate their efficiency and performance on toughening laminates.

Recently, elastomeric nanofibers based on "liquid" (uncrosslinked) rubber were proposed as new effective nanomaterials for hindering delamination and improving other properties, such as damping [31]. The effect of rubbery nanofibers on fracture response of composite laminates has been investigated in different aspects. Maccaferri et al. [32] investigated the influence of Nitrile Butadiene Rubber (NBR) and Polycaprolactone (PCL) blend nanofibers on hindering delamination and increasing damping capacity in CFRP laminates. The results showed a significant increase in the fracture toughness in mode I, up to +480 % in the initiation stage and up to +340 % in the propagation stage of

---

* Corresponding author.
E-mail address: tommasomaria.brugo@unibo.it (T.M. Brugo).

delamination, and a maximum enhancement in the mode II fracture toughness near 30 %. Povolo et al. [33] presented the effect of mat grammages and stacking sequence on damping behavior of CFRPs, appraised by dynamic mechanical analysis (DMA) tests. The single cantilever beam vibration tests showed 77 % enhancement in the damping capacity of the composite with only 1.5 % of weight increment.

Since delamination is often undetectable by visual inspection or very difficult to be monitored during mechanical tests, various non-destructive testing methods have been proposed to solve this problem: thermography, ultrasonic method and X-ray, which have their advantages and disadvantages [34]. Most of the methods for detecting delamination are active, while in passive methods such as acoustic emission, it is possible to monitor the system in real time. Another advantage of applying the acoustic emission method is its ability to distinguish different types of damage, such as matrix cracking, fiber breakage, fiber/matrix debonding, and delamination [35,36]. Different damage modes in composite materials can be detected excellently by AE technique. M. Saeedifar and D. Zarouchas [37] shows that each damage mode in composite materials usually produces AE signals with almost unique characteristics. For instance, low amplitude, low frequency, long duration, long rise time and large counts are usually associated with matrix cracking. R. Gutkin et al. [38] presented failure mechanism in CFRP by using acoustic emission method (AE). Five different types of test, such as tensile, compact tension, compact compression, DCB and ENF, were performed on CFRP laminates to determine the AE frequency of the five different damage modes.

So far, different studies have been conducted on composite laminates reinforced by rubbery nanofibers; however, no studies have been done to quantitatively evaluate the effect of the nanofibrous mat areal weight on mode I and II interlaminar fracture toughness and its toughening mechanism. The results obtained from this study provide valuable insights into the effect of NBR/PCL nanofibrous mat grammages on the fracture toughening of DCB (Double Cantilever Beam) and ENF (End-Notched Flexural) carbon fiber woven laminates. Furthermore, the interpretation of acoustic emission data by neural network combined with optical and SEM (Scanning Electron Microscope) micrograph analysis allowed a deeply interpretation of the toughening mechanism.

2. Materials and methods

2.1. Preparation of polymer solutions and blend electrospinning

The process procedure for fabricating rubbery nanofibers is visualized in Fig. 1. NBR solution (s-NBR, 10 % wt) was prepared in DMAc, e.g. 2.0 g of polymer in 19.2 mL of solvent. PCL solution (s-PCL, 10 % wt) was prepared in CHCl$_3$/DMF 50:50 wt, e.g. 2.0 g of polymer in 6.0 mL of CHCl$_3$ and 9.4 mL of DMF). Both polymer mixtures were stirred at room temperature (23–25 °C) until the formation of a homogeneous solution.

NBR/PCL blend (b-NBR/PCL) was prepared by mixing together the two starting solutions s-NBR and s-PCL in a 60:40 wt proportion, e.g. 6.0 g of s-NBR and 4.0 g of s-PCL. The blend was stirred at room temperature at least for 2 h to ensure proper homogenization. The blend has a 60 % wt of rubber content with respect to the total polymeric fraction. Table SI-1 lists the details of all the solutions prepared and their blend.

The parameters of electrospinning process are as follows: flow rate 1 ml/h, electric potential 22 kV, Distance between the collector and needles' tip 13.0 cm. Mats have final dimensions of approximately 30 × 40 cm. Electrospinning was conducted in the air atmosphere at 21–24 °C and 35–40 % relative humidity (RH). To enhance the process productivity 4 needles were used and to homogenize the nanofibrous grammage a drum collector connected to the ground was employed.

Four different thicknesses of the NBR/PCL blend nanofibrous mats were produced. The mat thickness was measured using an analogue indicator under 360 g/m^2 pressure. The resulting grammage was 9.6 g/m^2–18.1 g/m^2–39.2 g/m^2 and 54.8 g/m^2 for 20, 40, 80 and 120 μm nanomats, respectively. Morphology of the nanofibers is shown in the SEM micrograph of Fig. 2. The measured diameter ranges from 210 to 320 nm. Moreover, it can be observed that the nanofibers coalesce each other in crossing points, due to the low glass transition temperature (Tg) of the rubber.
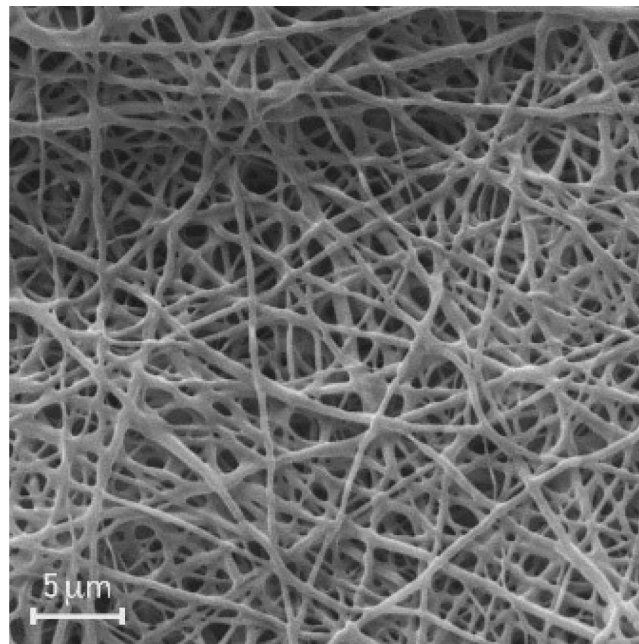

Fig. 2. SEM micrographs of electrospun NBR/PCL nanofibers (60:40 wt).
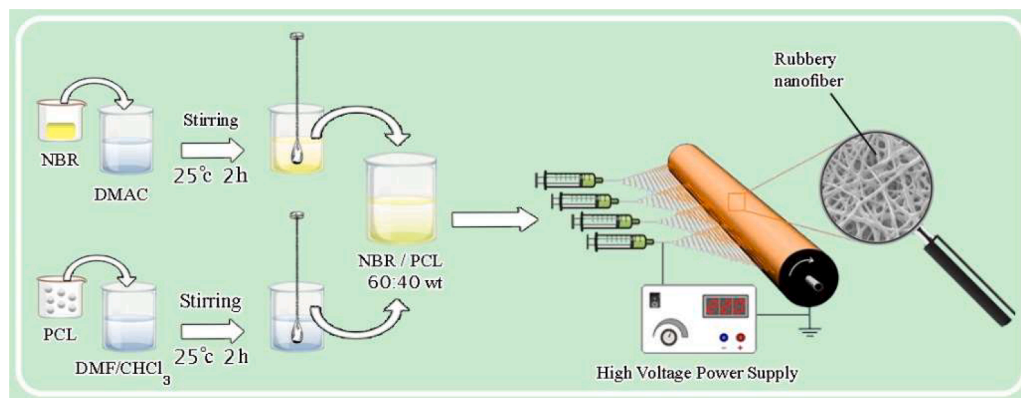

Fig. 1. A schematic of the preparation of polymer solutions and electrospinning process.

2.2. Specimen fabrication

The test samples were fabricated by 200 g/m^2 plain woven carbon/epoxy prepreg laminates. The number of layers used to fabricate the composite laminate was 14 (the final average thickness of the cured laminates was 3.6 mm). A thin Teflon film with a thickness of 13 μm was used to trigger an initial pre-crack. To make reinforced samples, nanofibers with a length of 6 cm were placed in the continuation of the initial pre-crack (Teflon layer). In fact, the Teflon and the nanofiber layer were placed in the mid-thickness of the manufactured laminate (between 7th and 8th layers). In order to prevent the penetration of resin in front of the pre-crack layer, about 1 cm of the nanofibrous mat was placed on the Teflon layer. Uncured panels were subjected to a preliminary treatment for 2 h at 45 °C under vacuum condition for better impregnation of nanofibers before the curing cycle in autoclave (2 h at 135 °C, under vacuum, 6 bar external pressure, heating/cooling ramp of 2 °C/min). To ensure that the process conditions were consistent for all the laminates, all the samples were cured in the same autoclave batch. Different type of laminates were fabricated, the pristine one without nanofibers named C-Ref and the nanomodified ones named C-20, C40, C-80, C-120 according to the relative thickness of the interleaved nanofibrous mat. In Fig. 3 the cross section of the fabricated laminates are shown. As can be observed no differences in the middle plane interlayer, where the nanofibers mat were interleaved, are visible. However, a slight increase on the overall thickness of the laminate can be observed with increasing of the nano-mat thickness, up to 124 um for the C-120 laminate. For each type of laminate the DCB and the ENF one were fabricated, for a total of 10 panels. From each panel, 3 specimens were extracted by using a high-speed rotating diamond saw with the dimensions depicted in Fig. 4.

2.3. Test method

Mode I and II tests were performed according to ASTM D5528 [37] and ASTM D7905 [38] standards, respectively. Geometry of the samples and the test set-up are depicted in Fig. 4. The test was performed in displacement control with a crosshead speed of 5 mm/min and 1.6 mm/min for DCB and ENF tests, respectively, by means of Instron 8033 servo hydraulic universal testing machine equipped with a 2 kN load cell.

DCB tests were carried out to evaluate the energy release rate for mode I loading (G_I, in J/m^2) at the initiation and propagation stages of delamination (G_{IC} and G_{IR}, respectively) using the following equation:

$$G_I = \frac{3P\delta}{2Ba} \tag{1}$$

In which P and δ are the load and opening displacement, respectively; B and a are the sample width and crack length, respectively. Fracture toughness in mode I is calculated by substituting the critical load, P_c, and its corresponding crack length, a_c, in Eq. (1).

ENF test has been performed to find strain energy release rate in mode II loading conditions. According to ASTM D7905 standard, compliance calibration parameters should be obtained by performing two initial tests with the initial crack length of 20 and 40 mm before conducting the final fracture test with a crack length of 30 mm. The important point is that the load applying to the sample in the initial tests should not exceed half of the maximum load in the final fracture test for preventing crack growth in the initial tests.

The G_{IIC} of ENF specimens is calculated as follows:

$$G_{IIC} = \frac{3mP_{cr}^2 a_0^2}{2B} \tag{2}$$

$$C = A + ma^3 \tag{3}$$

where P_{cr} represents the critical load corresponding to the crack growth, which is the maximum load in the load–displacement curve, a_0 and B indicate the initial crack length and the width of the sample, respectively; A and m are the compliance calibration coefficients, and C is compliance. To calculate the m coefficient, first, C value (the inverse of the slope of the initial linear elastic part of the load–displacement curve) must be calculated for the initial crack length of 20 mm, 30 mm and 40 mm. Then, the graph of C value as function of the cube of the initial crack length, can be drown as reported in Fig. 5. Afterward, by fitting a line to the obtained points, the compliance calibration coefficients are obtained according to Eq. (3).

AEWin software and PCI-2 system with a data sampling rate of 1Ms/s were used to record acoustic emission data. Two wideband single-crystal piezoelectric sensors, Nano-30, supplied by Physical Acoustics Company, were used. The resonant frequency of the sensor is 300 kHz and its optimal working range is 125–750 kHz. The gain selector of the pre-amplifier was set to 40 dB. Vacuum silicone grease was used to improve the transmission of the signal between the specimen and the sensor. To eliminate background noises during the tests, a threshold of 35 dB was considered.

2.4. Clustering method

Nowadays, clustering techniques are widely used in various industries for data mining. In this method, objects are grouped in such a way that similar objects are placed next to each other in a category [39]. In the past, methods for data clustering have been proposed, which had shortcomings such as dependency on center initialization, slow convergence rate, local optimal trap, and etc. For this purpose, several algorithms based on swarm intelligence have been introduced for clustering and their performance has been proven. Swarm intelligence is a field of computational intelligence that is used to develop multi-agent
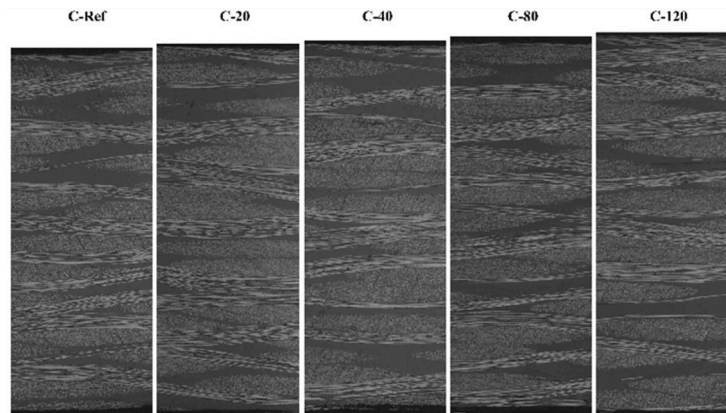

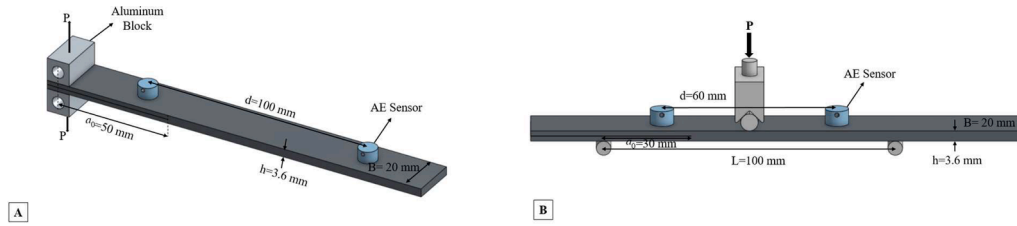**Fig. 3.** Cross section of fabricated laminate.

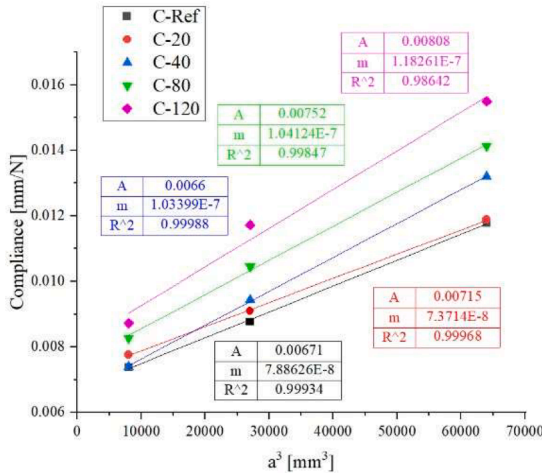**Fig. 4.** The dimensions of A) DCB and B) ENF specimens.

Fig. 5. Compliance calibration test of the non-modified and nano-modified ENF specimens.

intelligent systems inspired by life. This approach has modeled the cumulative behavior of natural factors such as flocks of birds, fishes or etc. to build algorithms. In this paper, the Artificial Bee Colony (ABC) algorithm is used as an optimization solution for clustering of acoustic emission data. The ABC algorithm was first presented in 2005 by

Karaboga [40] to optimize the real parameter inspired by the behavior of a bee colony. Additional explanations about this algorithm are given in the paragraph 3 of the supplementary information.

3. Results and discussion

In this section, the fracture test results, SEM micrographs and acoustic emission results are presented.

3.1. The effect of the nanofibers on the fracture toughness

The mechanical data recorded during the test are used to investigate the delamination behavior in the reference and modified samples toughened with 20, 40, 80, and 120 μm thick nanomat under mode I and mode II loadings.

3.1.1. Mode-I loading

Fig. 6-A illustrates the force-displacement curves of DCB tests. All curves show a comparable initial slope before crack propagation, which means that the interlayer toughening does not affect the specimen stiffness. However, the maximum load at the crack initiation was remarkably higher for all nanomodified specimens (50–60 N) compared to the reference one (35 N). After the first drop, in the crack propagation region, the reference, and the nano-interleaved C-20 and C-40 samples show a force displacement curve with a jagged profile, while for the C-80 and C-120 the curve appears smooth. The multiple force drops are usually attributed to a fragile crack propagation, while the smooth
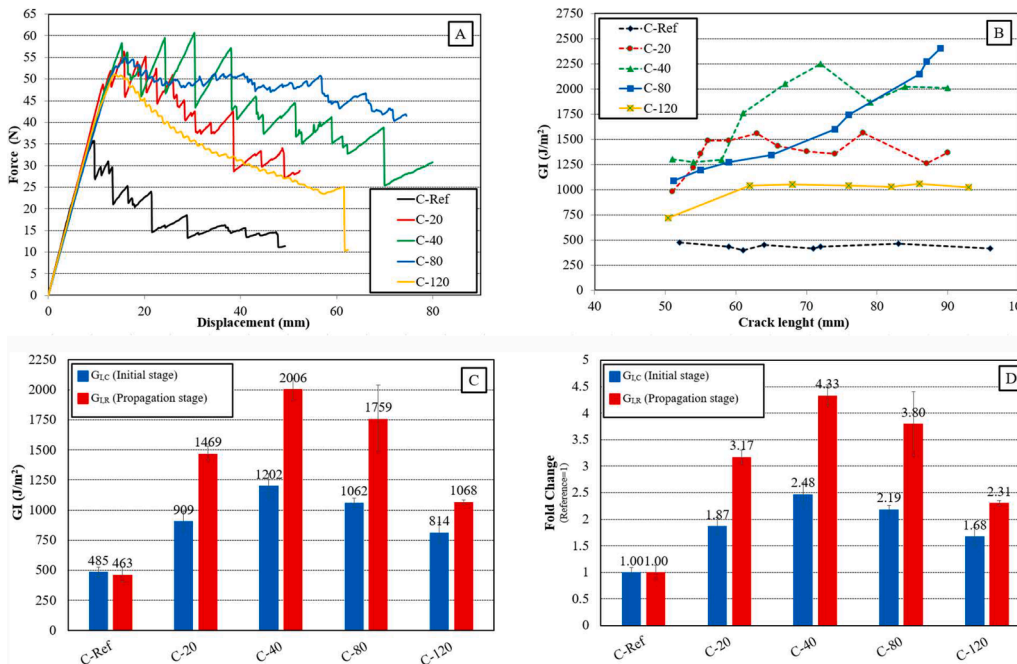

Fig. 6. DCB tests results: (A) load–displacement curves; (B) R-curves related to the same specimens displayed in (A); (C) average G_{IC} and G_{IR}; (D) G_I fold change (bars are expressed as the relative variation of the value with respect to the reference sample (C-Ref), whose value is set as 1.0).

propagation is characteristics of toughened materials.

Fig. 6-B shows the R-curve, i.e., the variation of fracture toughness during the crack propagation, of all specimens types, calculated at each load drop in the curves of Fig. 6A. The G_I curve trend for the reference and C-120 sample shows a plateau, while for the C-20, C-40 and C-80 it increases with the crack propagation. The increasing trend of R-curve is usually correlated to the crack bifurcating and carbon fiber tow breakage. Crack bifurcation increases the crack surface and hence energy absorbed during the crack propagation, while the breakage of carbon fiber requires high energy values.

In Fig 6-C, the fracture toughness values at the crack initiation (G_{IC}, calculated at the maximum force) and crack propagation (G_{IR}, calculated in the 60–80 mm crack length range) are shown. All nanomodified specimens show an increase in the fracture toughness compared to the reference one in both initiation and propagation stages. This increase can reach up to 148 % at the initiation and 333 % at the propagation stages. Investigating the effect of nanomat thickness shows that the maximum fracture toughness values are related to C-40 sample, and any further increase in the nanomat thickness does not lead to further improvement in the fracture toughness (C-80) or even decreases the fracture toughness (C-120). The higher fracture toughness enhancement at the crack propagation stage compared to the initiation stage could be attributed to the crack bifurcating phenomena.

3.1.2. Mode-II loading

Fig. 7 presents the mode II fracture test results for non-modified and nanomodified laminates. Fig. 7-A and B shows that the maximum load of C-20 and C-40 samples is 12 % and 7 % more than the reference sample, respectively. On the other hand, the maximum load of two other nanomodified samples reduced in comparison with the non-modified one. Moreover the stiffness of C-80 and C-120 samples is lower than the others, due to excessive toughening of the interlayer. Similar to the DCB test, the R-curves of the ENF tests are presented in Fig. 7-B. In this case due to the stable and continuous propagation of the crack (without remarkable force drops), the G_{II} at propagation was calculated at equally

spaced points of crack length with a 5 mm step. As can be observed, similar to G_I, G_{II} increased during the crack propagation. In Fig 7-C, the fracture toughness values at the crack initiation (G_{IIC}, calculated at the maximum force) and crack propagation (G_{IIR}, calculated in the 40–50 mm crack length range) are shown.

As shown in Fig. 7C and D, the energy release rate in both initiation and propagation stages increased by 28 % and 43 % for C-20 sample. Further increasing the thickness of the nanomat has a detrimental effect on the fracture toughness of the hoisting material. In particular, the 120 μm membrane leads to a 47 % decrease in the fracture toughness in the crack initiation stage. Generally, the fracture toughness enhancement by nanofiber interleaving at mode II is remarkably lower than mode I. Similar observations have been found in literature [41] for high toughened resin, in which the mode I interlaminar fracture toughness of the composite increased much more than mode II compared to the GI of the neat resin. This phenomenon has been attributed to load redistribution ahead of the crack tip for mode II due to microcracking ahead of the crack tip, which can be accomplished with fragile resins systems.

3.2. Micrograph analysis of the crack path

3.2.1. DCB specimen

Fig. 8 shows the micrographs of crack growth path in DCB specimens. In non-modified specimen (C-Ref), the crack propagates straight forward through the mid-plane interlayer, while the crack path for the rubbery nanomodified specimens is generally more complex, except for the C-120. In C-20, C-40 and C-80 laminates, the crack propagates linearly at the beginning through the interlayer where it was induced by the Teflon sheet; then the crack diverges to propagates in the not toughened adjacent interface. During crossing the adjacent layer, the crack breaks the high-strength carbon fiber reinforcement, absorbing energy, and bifurcates, increasing the crack surface area and hence further increasing the fracture energy, confirming the mechanical test results. Regarding C-120 sample, the high thickness of the nanomat leads to a decrease in the interlayer strength compared to C-40 and C-80 samples.
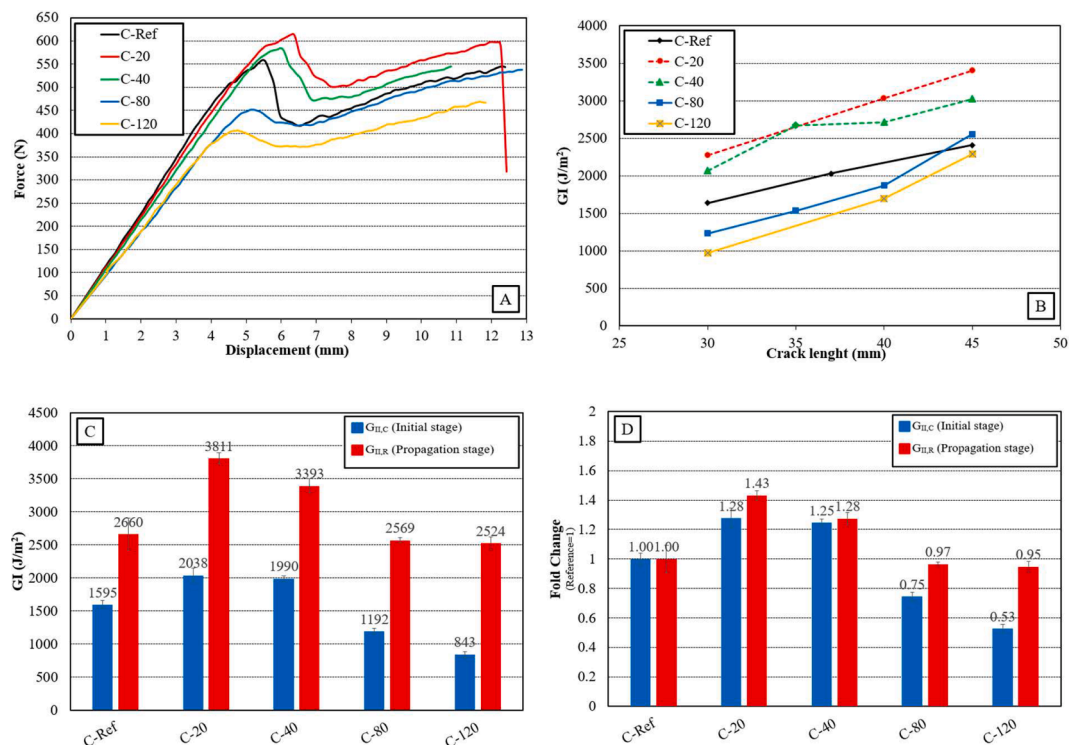

Fig. 7. ENF tests results: (A) load–displacement curves; (B) R-curves related to the same specimens displayed in (A); (C) average G_{ILC} and $G_{I,R}$; (D) G_I fold change (bars are expressed as the relative variation of the value with respect to the reference sample (C-Ref), whose value is set as 1.0).
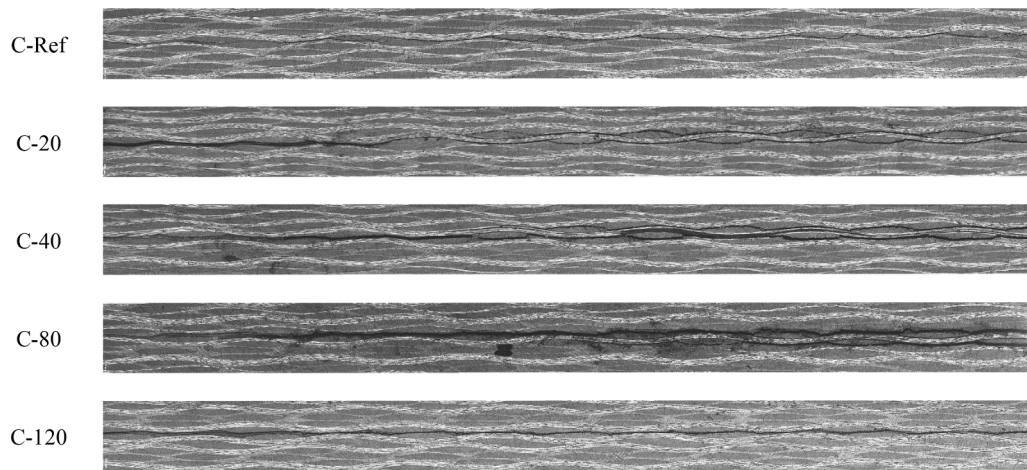
Fig. 8. Micrographs of DCB specimens after the tests.

Despite in the C-120 laminate the crack propagates smoothly through the mid-plane interlayer as the reference one the recorded fracture energy is higher. The cause of this discrepancy can be explained by the SEM surface micrograph analysis in the next paragraph.

3.2.2. ENF specimen

The effect of the rubbery nanofibers on the mode II delamination crack path is shown in Fig. 9. While the crack smoothly propagated in the reference laminate, the path displayed a jagged profile in most of the modified ones. The intensity of this profile is much more visible in C-20 and C-40 samples in comparison to the other ones. This phenomenon is related the fact that the crack tries to divert from toughened interlayer and propagates in the less-toughness adjacent layers. However, if the crack tends to propagate in the adjacent interfaces, it has to break the adjacent high-strength carbon fiber layer. In the case of the C-120 specimen, the interlaminar fracture toughness is reduced by the excessive amount of rubbery nanofibers and the crack propagates smoothly through it.

3.3. SEM micrograph analysis of the crack surface

To better understand the delamination behavior of the rubbery-modified composites with respect to the commercial non-modified CFRP, SEM investigation was carried out on both DCB and ENF delamination surfaces as shown in Fig. 10.

3.3.1. DCB specimens

Fig. 10A–J shows the SEM micrograph of the DCB samples fracture surface. The images in the same row refer to the same sample type. For each sample type, the left image is focused on the carbon fiber dominated zone of the fracture surface, and the right image is focused on the matrix dominated zone. It's worth of mentioning that, since the crack deviated to other layers in some samples, SEM micrographs were performed on the delamination surfaces before the crack divert. The reference sample shows completely clean carbon fibers, and the matrix-rich regions surfaces appear smooth, meaning a low adhesion of the resin to the carbon fiber. While after interleaving NBR/PCL nanofibers, the carbon fiber surface is not visible anymore, meaning an enhanced adhesion of the resin to the carbon fiber. Moreover, the crack surface appears jagged, typical of toughened resin systems. It can be observed that higher is the thickness of the nanomat and less visible are the carbon fibers, meaning a better fiber-matrix adhesion. Furthermore, in the resin-rich zone of the nanomodified samples voids are visible, which can be related to cleavage phenomenon. This behavior is typical of toughened matrix in which its high strain to break brings to voids nucleation in front of the crack tip, followed by their coalescence and finally crack propagation [42]. As consequence of this mechanism, the energy required for the crack propagation increases.

3.3.2. ENF specimens

As shown in Fig. 10K–S, similar to what observed for DCB delamination surfaces, the higher the interleaved mat thickness, the higher the
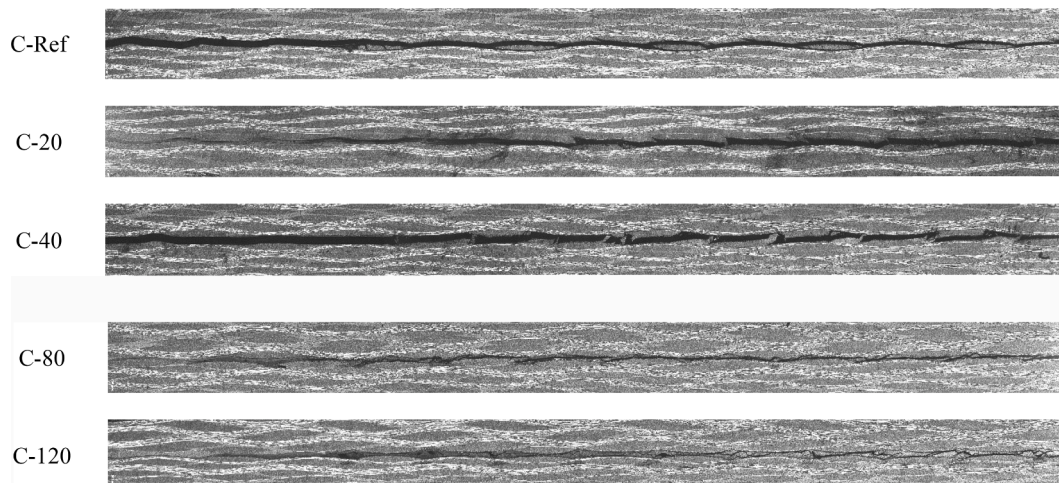

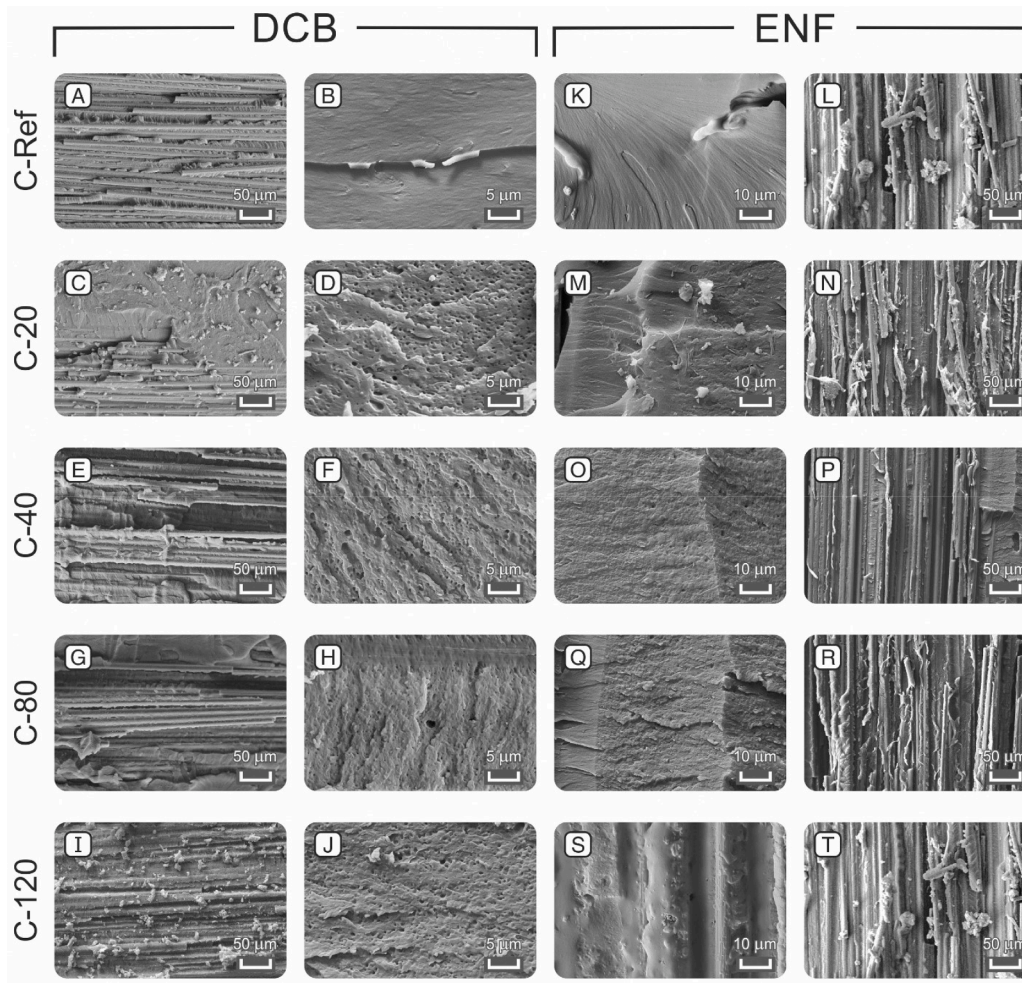**Fig. 9.** Micrographs of ENF specimens after the tests.

Fig. 10. Optical and SEM micrographs of delamination planes of DCB and ENF specimens after testing.

toughening effect on the matrix morphology, as visible focusing on the matrix-rich region taken from ENF specimens. The use of the highest mat thickness (C-120, Fig. 10S) leads to an extended matrix toughening so that "plastic" regions reminiscent of bulk rubber are present. While macroscopically the resin morphology between the carbon fibers is quite different, the fibers' aspect is in accordance with the observations done for the DCB delamination surfaces. Indeed, the unmodified interlayer displays clean carbon fibers, which becomes more affected by the toughened resin by increasing the interleaved nanofibers amount.

3.4. The effect of the nanofibers on the damage mechanisms

In the previous section, the effect of the thickness of rubbery nanofibers mat on the fracture toughness of CFRP samples was investigated using mechanical data and SEM images. In this section, acoustic emission is used to clarify how the rubbery nanofibers mat affects the dominant damage mechanisms of the CFRP samples. The flowchart of the acoustic emission data processing is depicted in Fig. 11. The details

of each step will be presented hereafter.

The eight main features, which are frequently used in the literature, are extracted from acoustic emission signals and presented in Table SI-2. Based on the data obtained from mode I and II test, the upper and lower limits of each features have been determined. In the next step, to eliminate the features that do not provide valuable information for data clustering, features with higher discrimination capability are selected among all the extracted features. As shown in Table SI-2, the features have different units and their ranges are completely different, therefore, they are not comparable directly. To solve this problem, all features should be normalized in the range of 0–1. To this aim, each feature is divided by its maximum value. Then, descriptive statistical analysis has been done using the box chart analysis. In this plot, five main parameters are shown, including: the median, the first quartile, the third quartile, and the data min and max. All data are shown with 96.8 % confidence interval in Fig. 12. Therefore, the five features with the most discriminating ability for further analysis are A, PCNTS, AVG FREQ, D, and R. Then, for easier manipulation and analysis, dimensional reduction
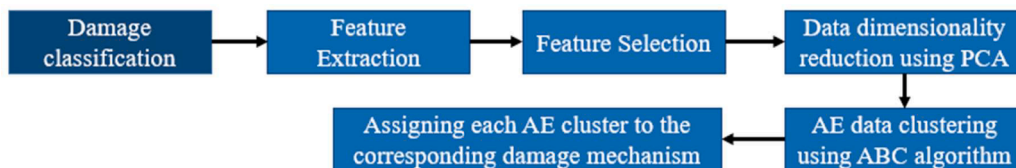

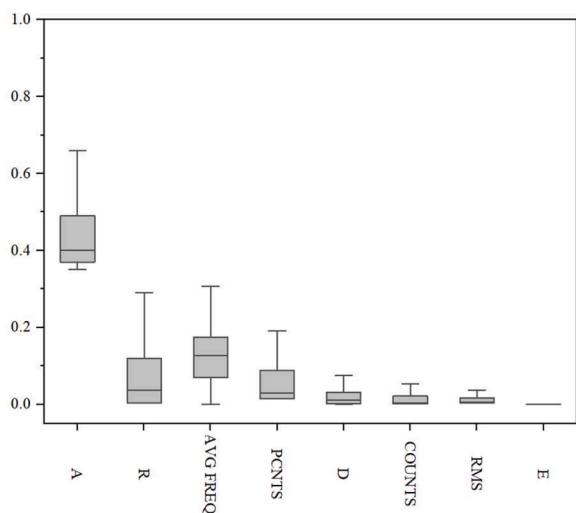**Fig. 11.** The proposed workflow for damage classification using acoustic emission.

Fig. 12. The results of a descriptive statistical analysis for the AE data of the DCB test.

should be done, for this purpose, Principal Component Analysis (PCA) method has been used for the five selected features. New independent variables (principal component) have been created using the PCA method to maximize the variance (increasing data discrimination potential). These variables are linear functions of the initial variables. The PCA method has more details that can be discovered in Pashmforoush et al. [35] As mentioned, five initial variables have been selected in this research (A, PCNTS, AVG FREQ, D, and R), so most of the information can be found in the first principal variable and then the rest in the second. The two principal components of the PCA for AE signals (PCA 1 and PCA 2) that lead to the most discrimination between AE dataset are shown in Fig. 13.

Then, the ABC algorithm was used to cluster the AE data into three clusters by minimizing the following objective function:

$$WCD = \sum_{j=1}^{k} \sum_{x \in C_j} d(x, m_j) = \sum_{i=1}^{n} \min_{1 \le j \le k} d(x_i, m_i)$$

Where k is the number of clusters, x illustrates a data point, C_j is cluster j, m_j demonstrates the centroid of cluster j, d is the Euclidean distance, and n indicates the total numbers of data. The algorithm stopped after the defined maximum number of iterations, which is set at 200.

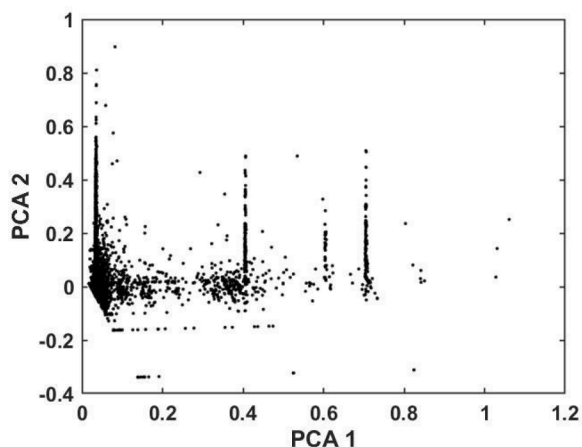While utilizing supervised classification, the training dataset determines the number of classes in advance. However, unsupervised clustering requires finding the best number of clusters and the Calinski–Harabasz criteria was employed. This method use an iterative optimization process to find the best number of clusters. The Calinski–Harabasz criterion defines the objective function as a function of the ratio of the variance between clusters to the variance within clusters [43]. The optimal number of clusters is indicated by the highest value of the Calinski–Harabasz criterion. As shown in Fig. 14 for the current AE dataset, the optimal number of clusters for the AE dataset is 3.

As example, Fig. 15 shows the resulting clustered data and the value of the objective function in each iteration for C-20. The ABC algorithm converged to the best clustering solution after ~40 iterations, as shown in Fig. 15A. Each cluster corresponds to a range of the amplitude. M. Fotouhi and M.A. Najafabadi has specified the corresponding range of amplitude for each type of fracture mechanism: matrix cracking, matrix/ fiber debonding and fiber breakage correlate to the lowest, average and highest amplitude ranges, respectively.

Fig. 16 summarize the results of AE clustered data, according to the procedure described above, for all types of laminates tested in Mode I (Fig. 16A) and II (Fig. 16B). The y-axis represents the fraction of events for each type of fracture mechanism (matrix/fiber debonding, fiber brakeage, matrix cracking), out of the total events that happened during the test. It is worth mentioning that since the crack deviated to other layers in some samples, acoustic emission data was analyzed up to the moment of the crack deviation. The AE evaluation was performed only in this range to focus on the effect of the toughening interlayer (where nanofibers were interleaved) and not when the crack divert from it and propagates in other non-toughened interlayers.

For mode-I (Fig. 16A), it can be observed that with increasing of the nanomat thickness the contribution of matrix cracking on the overall mechanism increases up to C-40 to then decrease for higher thickness. On the contrary, the matrix/fiber debonding decreases up to C-80 to then increase. Fiber brakeage seems to have no correlation with the nanomat thickness. In conclusion, by increasing the nanomat thickness up to 40–80 um the energy dissipated by matrix cracking increase, while fiber/matrix debonding decreases. AE findings correlate the mechanical results of Fig. 6, in which the G_{IC} increases by increasing the nanomat thickness up to 40 μm to then decrease (in agreement with matrix cracking trend), and the SEM micrographs of Fig. 10, in which the adhesion of the matrix is enhanced by the nanofibers interleaving (hence a decrease of the matrix / fiber debonding) and the crack surface appears more jagged (meaning an increase of absorbed energy by matrix cracking). On the contrary, as observed by the SEM micrographs of the fracture surfaces of Fig. 10, the amount of broken fibers has no correlation with the nanomat thickness.

Fig. 16-B illustrates the percentage of different damage mechanisms under mode-II loading conditions. Generally, slightly changes were observed in AE results, confirming the mechanical results reported in Fig. 7. Indeed, matrix/fiber debonding is comparable for the in C-Ref, C-20, and C-40 samples, while the slightly increase for the C-80 and C-120.

4. Conclusion

In this study, the influence of NBR/PCL nanofiber mat thickness (20 μm, 40 μm, 80 μm, and 120 μm) on fracture behavior and various damage modes, i.e. matrix cracking, fiber/matrix debonding, and fiber breakage, is investigated. For a deep consideration, SEM micrographs, AE analysis, and optical microscope was also applied. The following results were concluded:

1- NBR/PCL blend nanofibers could considerably increase the fracture toughness although their effectiveness was more remarkable for mode-I fracture load.
2- The optimum thickness of nanofibrous mat was 40 μm and 20 μm in mode-I and mode-II loading, respectively. It should be mentioned that increasing the thickness from 20 μm to 40 μm did not cause a high reduction of fracture toughness during mode-II. Therefore, 40

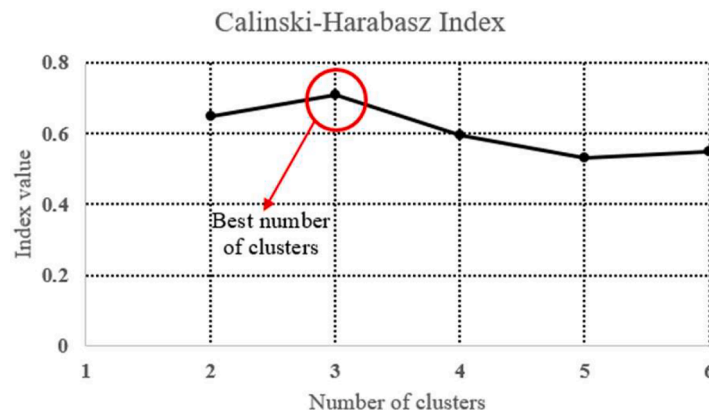**Fig. 13.** The PCA components for the AE data of the DCB test.

Fig. 14. Specifying the best number of clusters using Calinski–Harabasz indices.
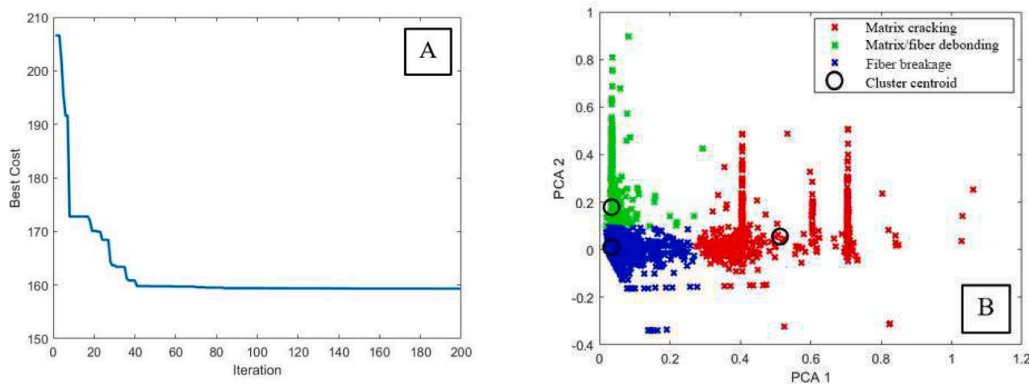

Fig. 15. (A) The objective function value in different iterations and (B) the clustered AE data.
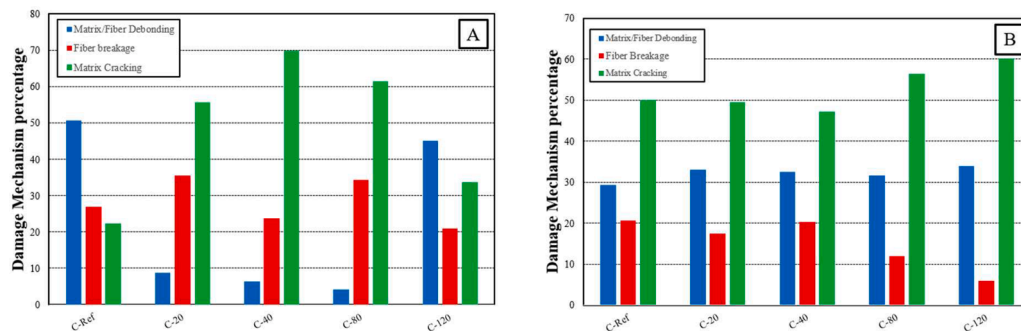

Fig. 16. Conversion of the damage mechanism in (A) DCB (B) ENF.

μm nanomat thickness can be chosen as the optimum thickness for both modes.

3- SEM micrograghs of sample tested under mode-I loading showed that cleavage phenomenon is visible in resin-rich area which is a typical behavior in toughened matrix.

4- AE analysis of DCB specimens proved that interleaving nanofibers caused significant decrease in fiber/matrix debonding except in C-120 which has similar behavior with the reference; on the other hand it led to increase in matrix cracking.

5- The trend of AE data is different in ENF samples. Interleaving the nanofibers caused slight increase in fiber/matrix debonding while fiber breakage decreased. This reduction is remarkably high for C-120 sample.

In conclusion, a toughening threshold for mode I and II was found for rubbery nanofiber interleaving thickness. This behavior was explained by the antithetic effects between toughening and strength of the interleaved interface. The observation were confirmed by SEM and AE emission analysis.

CRediT authorship contribution statement

Jacopo Ortolani: Writing – original draft, Project administration, Visualization. **Francesco Mongioì:** Writing – original draft, Visualization, Data curation. **Laura Mazzocchetti:** Supervision, Resources. **Andrea Zucchelli:** Supervision, Funding acquisition.

Declaration of competing interest

The authors declare that they have no known competing financial interests or personal relationships that could have appeared to influence the work reported in this paper.

Acknowledgment

Supplementary materials

Supplementary material associated with this article can be found, in the online version, at doi:10.1016/j.tws.2024.111556.

References

[1] N. Li, Y. Zhou, Failure mechanism analysis of fiber-reinforced polymer composites based on multi-scale fracture plane angles, Thin-Walled Struct. 158 (2021) 107195.

[2] J. van de Kerk, R.F. de Melo, G. Bastiani, M.V. Donadon, M.A. Arbelo, A numerical and experimental study of fasteners as a delamination arrest mechanism in composite laminates under mode I loading, Thin-Walled Struct. 191 (2023) 111047.

[3] N. I.O.B.-S.L. Sela, Toughness improved high performance torayca prepreg T800H/3900 series. 33rd Int. SAMPE Symp, Society for the Advancement of Material and Process Engineering, 1988, pp. 272–283.

[4] N. Sela, O. Ishai, L. Banks-Sills, The effect of adhesive thickness on interlaminar fracture toughness of interleaved CFRP specimens, Composites 20 (3) (1989) 257–264.

[5] N. Pagano, R.B. Pipes, The influence of stacking sequence on laminate strength, J. Compos. Mater. 5 (1) (1971) 50–57.

[6] A. Pereira, A. De Morais, Mode I interlaminar fracture of carbon/epoxy multidirectional laminates, Compos. Sci. Technol. 64 (13–14) (2004) 2261–2270.

[7] N. Pai, A. Kaw, M. Weng, Optimization of laminate stacking sequence for failure load maximization using Tabu search, Compos. Part B: Eng. 34 (4) (2003) 405–413.

[8] R. Wei, G. Pan, J. Jiang, K. Shen, D. Lyu, An efficient approach for stacking sequence optimization of symmetrical laminated composite cylindrical shells based on a genetic algorithm, Thin-Walled Struct. 142 (2019) 160–170.

[9] L. Mignery, C. Sun, T. Tan, The use of stitching to suppress delamination in laminated composites, ASTM International (1985).

[10] G.-C. Tsai, J.-W. Chen, Effect of stitching on mode I strain energy release rate, Compos. Struct. 69 (1) (2005) 1–9.

[11] L. Francesconi, F. Aymerich, Numerical simulation of the effect of stitching on the delamination resistance of laminated composites subjected to low-velocity impact, Compos. Struct. 159 (2017) 110–120.

[12] M.B. Dow, Development of stitched, braided and woven composite structures in the ACT program and at Langley Research Center. National Aeronautics and Space Administration, Langley Research Center, 1997.

[13] Z. Wu, J. Li, L. Shi, X. Chen, Effect of stacking configuration on the mechanical property and damage behavior of braided composite tube under three-point bending, Thin-Walled Struct. 187 (2023) 110762.

[14] W. Howard, J. Gossard, R.Jones Terry, Reinforcement of composite laminate free edges with U-shaped caps, in: 27th Structures, Structural Dynamics and Materials Conference, 1986, p. 972.

[15] W.S. Chan, O. Ochoa, Edge delamination resistance by a critical ply termination, Key Eng. Mater. (1989) 285–304. Trans Tech Publ.

[16] A. Yudhanto, N. Watanabe, Y. Iwahori, H. Hoshi, Compression properties and damage mechanisms of stitched carbon/epoxy composites, Compos. Sci. Technol. 86 (2013) 52–60.

[17] Y.A. Dzenis, D.H. Reneker, Delamination Resistant Composites Prepared By Small Diameter Fiber Reinforcement At Ply Interfaces, Google Patents, 2001.

[18] M. Saeedifar, H. Saghafi, R. Mohammadi, D. Zarouchas, Temperature dependency of the toughening capability of electrospun PA66 nanofibers for carbon/epoxy laminates, Compos. Sci. Technol. 216 (2021) 109061.

[19] R. Mohammadi, M.A. Najafabadi, H. Saghafi, D. Zarouchas, Mode-II fatigue response of AS4/8552 carbon/epoxy composite laminates interleaved by electrospun nanofibers, Thin-Walled Struct. 154 (2020) 106811.

[20] C. Garcia, J. Wilson, I. Trendafilova, L. Yang, Vibratory behaviour of glass fibre reinforced polymer (GFRP) interleaved with nylon nanofibers, Compos. Struct. 176 (2017) 923–932.

[21] P. Akangah, S. Lingaiah, K. Shivakumar, Effect of Nylon-66 nano-fiber interleaving on impact damage resistance of epoxy/carbon fiber composite laminates, Compos. Struct. 92 (6) (2010) 1432–1439.

[22] S. Cai, Y. Li, H.-Y. Liu, Y.-W. Mai, Damping properties of carbon fiber reinforced composites hybridized with polysulfone (PSF)/cellulose nanocrystal (CNC) interleaves, Compos. Sci. Technol. 213 (2021) 108904.

[23] P. Li, D. Liu, B. Zhu, B. Li, X. Jia, L. Wang, G. Li, X. Yang, Synchronous effects of multiscale reinforced and toughened CFRP composites by MWNTs-EP/PSF hybrid nanofibers with preferred orientation, Compos. Part A: Appl. Sci. Manuf. 68 (2015) 72–80.

[24] H. Saghafi, A. Nikbakht, R. Mohammadi, D. Zarouchas, The thickness effect of psf nanofibrous mat on fracture toughness of carbon/epoxy laminates, Materials (Basel) 14 (13) (2021) 3469.

[25] H. Taheri, M. Oliaei, H. Ipakchi, H. Saghafi, Toughening phenolic composite laminates by interleaving hybrid pyrolytic carbon/polyvinyl butyral nanomat, Compos. Part B: Eng. 191 (2020) 107981.

[26] H. Saghafi, A. Moallemzadeh, A. Zucchelli, T. Brugo, G. Minak, Shear mode of fracture in composite laminates toughened by polyvinylidene fluoride nanofibers, Compos. Struct. 227 (2019) 111327.

[27] P.K. Barzoki, A. Rezadoust, M. Latifi, H. Saghafi, G. Minak, Effect of nanofiber diameter and arrangement on fracture toughness of out of autoclave glass/phenolic composites-experimental and numerical study, Thin-Walled Struct. 143 (2019) 106251.

[28] H. Ipakchi, A.M. Rezadoust, M. Esfandeh, M. Rezaei, An investigation on the effect of polyvinyl butyral interlayer forms on the fracture toughness of glass reinforced phenolic laminates, Thin-Walled Struct. 151 (2020) 106724.

[29] S. van der Heijden, L. Daelemans, T. Meireman, I. De Baere, H. Rahier, W. Van Paepegem, K. De Clerck, Interlaminar toughening of resin transfer molded laminates by electrospun polycaprolactone structures: effect of the interleave morphology, Compos. Sci. Technol. 136 (2016) 10–17.

[30] J. Jang, J. Lee, Y.-J. Seol, Y.H. Jeong, D.-W. Cho, Improving mechanical properties of alginate hydrogel by reinforcement with ethanol treated polycaprolactone nanofibers, Compos. Part B: Eng. 45 (1) (2013) 1216–1221.

[31] E. Maccaferri, L. Mazzocchetti, T. Benelli, T.M. Brugo, A. Zucchelli, L. Giorgini, Self-assembled NBR/nomex nanofibers as lightweight rubbery nonwovens for hindering delamination in epoxy CFRPs, ACS Appl. Mater. Interfaces 14 (1) (2021) 1885–1899.

[32] E. Maccaferri, L. Mazzocchetti, T. Benelli, T.M. Brugo, A. Zucchelli, L. Giorgini, Rubbery nanofibrous interleaves enhance fracture toughness and damping of CFRP laminates, Mater. Des. 195 (2020) 109049.

[33] M. Povolo, E. Maccaferri, D. Cocchi, T.M. Brugo, L. Mazzocchetti, L. Giorgini, A. Zucchelli, Damping and mechanical behaviour of composite laminates interleaved with rubbery nanofibers, Compos. Struct. 272 (2021) 114228.

[34] H. Tuo, T. Wu, Z. Lu, X. Ma, B. Wang, Study of impact damage on composite laminates induced by strip impactor using DIC and infrared thermography, Thin-Walled Struct. 176 (2022) 109288.

[35] F. Pashmforoush, R. Khamedi, M. Fotouhi, M. Hajikhani, M. Ahmadi, Damage classification of sandwich composites using acoustic emission technique and k-means genetic algorithm, J. Nondestruct. Eval. 33 (4) (2014) 481–492.

[36] R. Khamedi, S. Abdi, A. Ghorbani, A. Ghiami, S. Erden, Damage characterization of carbon/epoxy composites using acoustic emission signals wavelet analysis, Compos. Interfaces 27 (1) (2020) 111–124.

[37] A. ASTM, Standard D5528-01: Standard Test Method For Mode I Interlaminar Fracture Toughness of Unidirectional Fiber-Reinforced Polymer Matrix Composites, ASTM International, West Conshohocken, PA, 2007.

[38] A. Standard, D7905/D7905m-14, Standard Test Method For Determination of the Mode II Interlaminar Fracture Toughness of Unidirectional Fiber-Reinforced Polymer Matrix Composites, ASTM International, West Conshohocken, PA, 2014, https://doi.org/10.1520/D7905_D7905M-14, 2014.

[39] S. Landau, M. Leese, D. Stahl, B.S. Everitt, Cluster Analysis, John Wiley & Sons, 2011.

[40] D. Karaboga, An idea based on honey bee swarm for numerical optimization, Technical report-tr06, Erciyes university, engineering faculty, computer …, 2005.

[41] W.L. Bradley, Relationship of matrix toughness to interlaminar fracture toughness, Composite Materials Series (1989) 159–187.

[42] T. Anderson, T. Anderson, Fracture mechanics: Fundamentals and Applications, 10, CRC press, Taylor and Francis Group, 2005, pp. 0–8493, 2005ISBN.

[43] T. Caliński, J. Harabasz, A dendrite method for cluster analysis, Commun. Stat. Theory Methods 3 (1) (1974) 1–27.